

An Isolated Three-Port Bidirectional DC-DC Converter With Decoupled Power Flow Management

Chuanhong Zhao, *Student Member, IEEE*, Simon D. Round, *Senior Member, IEEE*, and Johann W. Kolar, *Senior Member, IEEE*

Abstract—An isolated three-port bidirectional dc-dc converter composed of three full-bridge cells and a high-frequency transformer is proposed in this paper. Besides the phase shift control managing the power flow between the ports, utilization of the duty cycle control for optimizing the system behavior is discussed and the control laws ensuring the minimum overall system losses are studied. Furthermore, the dynamic analysis and associated control design are presented. A control-oriented converter model is developed and the Bode plots of the control-output transfer functions are given. A control strategy with the decoupled power flow management is implemented to obtain fast dynamic response. Finally, a 1.5 kW prototype has been built to verify all theoretical considerations. The proposed topology and control is particularly relevant to multiple voltage electrical systems in hybrid electric vehicles and renewable energy generation systems.

Index Terms—Bidirectional, decoupled power flow management, optimum operating point, three-port converter.

I. INTRODUCTION

RECENTLY, demand for versatile energy management systems capable of capturing energy from diverse sustainable and/or conventional energy sources, along with energy storage elements, is increasing because of their potential applications in hybrid electric vehicles (HEVs) and fuel cell vehicles (FCVs) [1], renewable energy generation systems [2], and uninterruptible power supplies. The voltage levels and the voltage-current characteristics of energy sources and storage devices are normally different from those of loads. Therefore, a multi-port converter interfacing sources, storages and loads needs to be incorporated into the entire energy management system.

In electric vehicle applications, energy storage elements [3] enable the capture of regenerative brake and energy release during startup and acceleration. A multi-port converter accommodates diverse energy sources and storages, and combines their advantages. Bidirectional power flow capability for the ports interconnecting storages is a key feature of the multi-port converter. Such a multi-port converter can also be employed in the multiple voltage electrical power distribution system in HEVs and FCVs. In order to meet the increasing power load demand, 42-V bus [4], [5] is introduced in the electrical system

and will replace the existing 14-V bus to provide power for all auxiliary components. Changing from 14 to 42 V can only be phased gradually from a practical point of view and during the transition it will be necessary to employ a dual low voltage system [6], [7]. Additionally, a high voltage (H.V.) bus such as 300 V, is required for the electric propulsion system of a HEV or a FCV. Therefore, a multiple voltage (14 V/42 V/H.V.) electrical system will likely be employed in HEVs and FCVs. Apart from the bidirectional power flow capability, the system requires the galvanic isolation between the low voltage and high voltage buses for safety reasons, although the isolation is not normally required between the low voltages of 14 and 42 V. Furthermore, for a system with N ports, $N - 1$ control variables are necessary in order to independently control the power flow of each port in an autonomous system.

Since a dc-dc converter can connect any two ports, it is natural to think of linking N ports up either by N individual dc-dc conversion stages with a common dc bus where energy from all ports is exchanged, or even simpler, by only $N - 1$ conversion stages with the use of one port as the common dc bus. These conversion stages are controlled independently and a communication bus may be needed for the purpose of managing power flow. Here an integrated multi-port converter, which utilizes a single power conversion stage to interconnect all ports, instead of the individual dc-dc conversion stages, can be introduced in order to make the whole system simpler. Thus, cost, size, and volume can be reduced due to less amount of devices and associated circuits. The reduced conversion step results in higher power density and efficiency. Moreover, the complicated communication that would be necessary between these individual conversion stages can be eliminated due to centralized control.

A few integrated multi-port dc-dc converter topologies are found in the literature. There are two categories for the integrated isolated multi-port converter. One type of converter involves a transformer in which there is a separate winding for each port, as shown in Fig. 1(a), therefore, all ports are fully electrically isolated [8]–[13]. The other type has a reduced parts count where some windings are absent, as illustrated in Fig. 1(b), if the system allows the corresponding ports to share a common ground [14]–[20]. However, in most applications the voltage magnitudes of ports are substantially different. For example, in renewable energy generation systems, safe, extra low voltage batteries or supercapacitors are preferable since fewer storage units are connected in series and fewer voltage balancing circuits are required. Adjustment of the voltage levels via the transformer turns ratio is beneficial in order to avoid the device handling both high voltage and high current simultaneously. This paper focuses on converters where all ports are fully isolated.

Manuscript received December 12, 2007; revised March 01, 2008. Current version published November 21, 2008. Recommended by Associate Editor S. Y. Hui.

The authors are with the Power Electronic Systems Laboratory, ETH, Zurich 8092, Switzerland (e-mail: zhao@lem.ee.ethz.ch; round@lem.ee.ethz.ch; kolar@lem.ee.ethz.ch).

Color versions of one or more of the figures in this paper are available online at <http://ieeexplore.ieee.org>.

Digital Object Identifier 10.1109/TPEL.2008.2002056

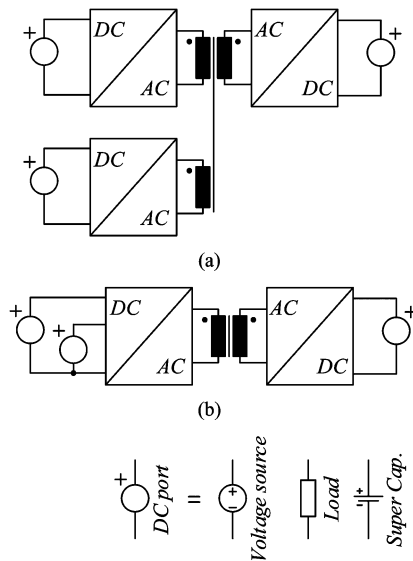


Fig. 1. Two types integrated isolated multi-port converter. (a) A transformer with a separate winding for each port is involved. (b) A transformer with a reduced number of windings is employed since the system allows some ports to share a common ground.

A method based on a time share concept has been proposed in [8]. Here, only one port is allowed to transfer energy from/to the common magnetic component at a time. Thus, the power rating is limited. The converter based on flux additivity in a multi-winding transformer is described in [9]. Although this topology has the capability of simultaneous power transfer, the reverse-blocking diodes only allow unidirectional power flow and prevent it from the applications where energy storage elements are needed. A converter topology, viewed as an extension of the boost-dual-half bridge topology [21], has been described in [10]. The converter presents the natural property of being bidirectional in the power flow. Although the existence of boost inductor reduces the port current ripple, it increases system cost, size, and limits the system bandwidth, thus slows the system dynamic response. Furthermore, a resonant converter topology is developed in [11], but it is not easy to implement.

Derived from the dual-active-bridge topology [22], a multi-port converter employing a multi-winding transformer is proposed in [12] and [13], as shown in Fig. 2. The high-frequency transformer not only integrates and exchanges the energy from/to all ports, but also provides full isolation among all ports and matches the different port voltage levels. A bidirectional power flow can be managed by adjusting the phase-shift angle between the high-frequency ac voltages generated by the full-bridge cell at each port. For a wide voltage variation, the multi-port converter cannot operate optimally since there are high peak/rms currents which lead to high conduction losses, and even the loss of soft-switching in some cases. The improved method, presented in [23], of continuously adjusting the duty cycle on one port according to its voltage level works satisfactorily. However, it loses soft switching immediately when more than one power source/storage element are involved. The idea in [24] is that a multi-port converter composed of half-bridge cells instead of full-bridge cells operates under phase shift in combination with pulse-width-modulation control technology. Again, this converter can only be used in the applications where only one

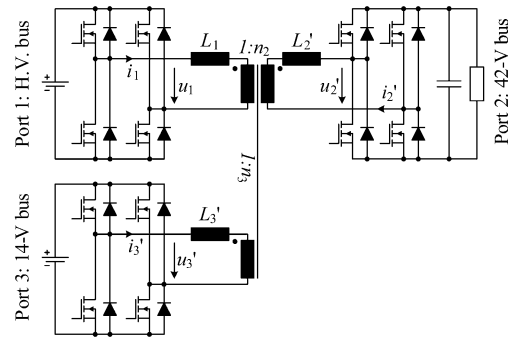


Fig. 2. Proposed isolated three-port bidirectional converter, where high frequency linking of the full-bridge cells is realized via a single transformer.

power source or storage is interconnected since the same duty cycle is used in all the half-bridge cells and is the only variable that can compensate for the variation of the voltage level.

This paper presents an optimization method for the topology depicted in Fig. 2 with the aim of minimizing the overall system losses, where zero circulating power within the converter is ensured, and the variation of the duty cycle at each port reduces the switching losses for port voltage variations. This feature allows efficient power conversion, low weight and low volume construction. Additionally, the small signal model of the system and the associated control design of the converter are developed. Due to the employment of the decoupling network, the multivariable control system can be decomposed into a series of independent single-loop subsystems, where the loop interaction can be eliminated. Therefore, high bandwidth for each control loop and fast dynamic response are achievable. A prototype of the multi-port converter has been built and successfully tested. The experimental results confirm the theoretical analysis and show the decoupling and good dynamic response. The proposed converter is a good candidate for the multiple voltage electrical system in HEVs and FCVs, and has distinct advantages of full isolation, bidirectional power flow, high efficiency and low weight.

II. CONTROLLABILITY OF THE POWER FLOW IN THE THREE-PORT CONVERTER

A. Topology Description and Equivalent Circuit of a Three-Winding Transformer

Fig. 2 shows the proposed multi-port converter, where the H.V. bus (port 1), 42 V-bus (port 2), and 14-V bus (port 3) are coupled via a three-winding transformer and corresponding full-bridge cells. A traction motor, for example, can be connected to the H.V. bus through an inverter. The energy storage elements, such as batteries and supercapacitors, can be interfaced with the dual low voltage buses, i.e., 14- and 42-V bus. The transformer has two functions: one is providing electrical isolation between these buses and the second is that different voltage levels in the buses can be matched by the suitable turns ratios. Since the current flowing in a full bridge cell can be bidirectional, this topology has bidirectional power flow capability. For example, 14-V bus can be charged by the energy generated from the generator (H.V. bus). On the other hand, it can also provide power to 42-V bus during start up when needed.

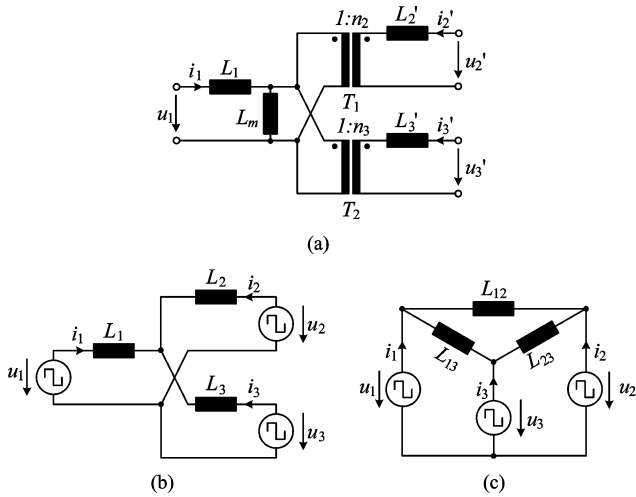


Fig. 3. (a) Equivalent circuit of a three-winding transformer. (b) Y-type primary-referred equivalent circuit of the proposed converter used for analyzing the dependency of the power transfer between the ports on the control signal phase displacements. (c) Δ -type primary-referred equivalent circuit of the three-port system.

The equivalent circuit of a three-winding transformer given in [25], is shown in Fig. 3(a), where L_m is the effective magnetizing inductance and T_1 and T_2 are two ideal transformers with turns ratios $1 : n_2$ and $1 : n_3$. The transformer leakage inductance which determine the power transfer in connection with the phase displacements of the individual full-bridge cell control signals are represented by L_1 , L_2' , and L_3' .

B. Direction of the Converter Power Flow

To determine the power flow in the converter, we will represent the output voltages of the full-bridge cells by the square wave voltage sources u_1 , u_2' , and u_3' with a duty cycle of 0.5. L_2' , i_2' , u_2' , V_2' , and L_3' , i_3' , u_3' , V_3' are referred to the primary side (H.V. bus) of the transformer, and represented by $L_2 = L_2'/n_2^2$, $i_2 = i_2'n_2$, $u_2 = u_2'/n_2$, $V_2 = V_2'/n_2$, and $L_3 = L_3'/n_3^2$, $i_3 = i_3'n_3$, $u_3 = u_3'/n_3$, $V_3 = V_3'/n_3$, respectively, where V_2' and V_3' are the dc voltage level of 42- and 14-V bus, and i_1 , i_2' , i_3' are the leakage inductance currents of each winding. Furthermore, we neglect the transformer magnetizing inductance L_m . The resulting equivalent circuit of the proposed system is shown in Fig. 3(b). The phase shift of the control signals of two full-bridge cells (the square wave voltage sources u_1 and u_2) is denoted as ϕ_2 in the following; accordingly, ϕ_3 denotes the phase displacement of u_1 and u_3 . There, ϕ_2 and/or ϕ_3 are defined as positive when u_1 is leading u_2 and/or u_1 is leading u_3 . The control range of ϕ_2 and ϕ_3 is from $-\pi/2$ to $\pi/2$.

The three-port converter can be simplified to a two-port converter if the third port is open. Based on [22] we then have for the power flow between two phase-shift controlled full-bridge cells [cf. Fig. 4(a)]

$$P_{12} = \frac{\phi_2(\pi - \phi_2)V_1V_2}{2\pi^2f_s(L_1 + L_2)} \quad (1)$$

where V_1 and V_2 are the magnitudes of u_1 and u_2 , and f_s denotes the switching frequency. According to (1) the amount and direction of the power flow is determined by the phase shift ϕ_2 .

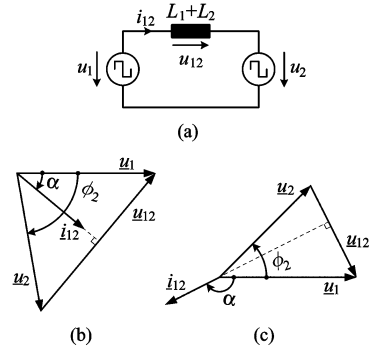


Fig. 4. (a) Equivalent circuit for studying the power flow between two ports when the third port is open. (b) Fundamental phasor diagram of the voltages and currents when $\phi_2 > 0$. (c) Fundamental phasor diagram of the voltages and currents when $\phi_2 < 0$.

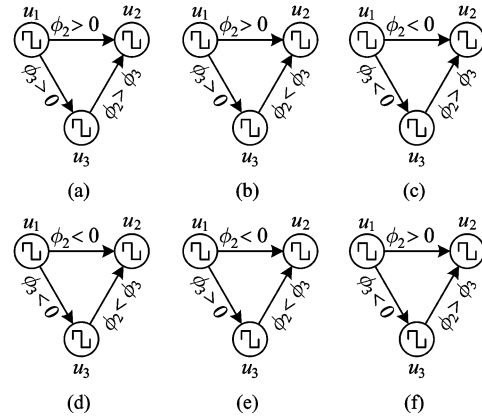


Fig. 5. Equivalent circuit for studying the power flow between three ports. The direction of power flow is only determined by ϕ_2 , ϕ_3 , not by V_1 , V_2 , and V_3 .

This is also immediately clear from fundamental phasor diagrams of the voltages and currents which are depicted in Fig. 4(b) and (c). \underline{u}_1 and \underline{u}_2 are the fundamental components of u_1 and u_2 . The fundamental power transferred from port 1 (u_1) to port 2 (u_2) is

$$P_{12} = \frac{1}{2}\hat{U}_1\hat{I}_{12}\cos(\alpha) = \frac{1}{2}\hat{U}_1\frac{\hat{U}_{12}}{\omega_s(L_1 + L_2)}\cos(\alpha) \quad (2)$$

where $\hat{U}_1 = 4V_1/\pi$, $\hat{U}_2 = 4V_2/\pi$, \hat{U}_{12} is the magnitude of $\underline{u}_{12} = \underline{u}_1 - \underline{u}_2$, $\omega_s = 2\pi f_s$, α denotes the phase displacement of \underline{u}_{12} and the current \hat{i}_{12} which is perpendicular to \underline{u}_{12} . For $\phi_2 > 0$ [cf. Fig. 4(b)], in case u_1 is leading u_2 , α is smaller than $\pi/2$. Therefore, we have $P_{12} > 0$, the power flow is physically oriented from port 1 (u_1) to port 2 (u_2) and it reverses for $\phi_2 < 0$ since α then is larger than $\pi/2$ [cf. Fig. 4(c)].

The Y-type primary-referred equivalent circuit depicted in Fig. 3(b) can be transformed into a Δ -type equivalent circuit shown in Fig. 3(c) which allows the resulting power flow of the three-port system to be determined by superposition of the power transfer of three two-port systems u_1, u_2, u_1, u_3 , and u_2, u_3 . For example, for $\phi_2 > 0$, $\phi_3 > 0$, and $\phi_2 > \phi_3$ [cf. Fig. 5(a)] the power flow is from u_1 to u_2 , u_1 to u_3 and u_3 to u_2 as $\phi_2 > \phi_3$. Therefore, u_1 is acting as a source and u_2 is consuming power. Dependent on the relation of ϕ_2 and ϕ_3 , port 3 (u_3) can be sinking or sourcing power or remain at zero power.

In summary, a power transfer is possible in any direction between any ports and the direction is only determined by ϕ_2 , ϕ_3 , not by V_1 , V_2 , and V_3 (cf. Fig. 5).

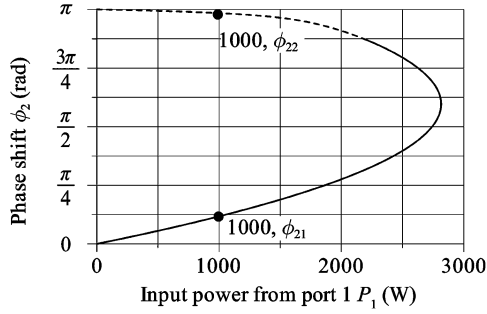


Fig. 6. Phase shift ϕ_2 for achieving $P_1 = -P_2 = 1$ kW and $P_3 = 0$ with the electrical parameters shown in Table I.

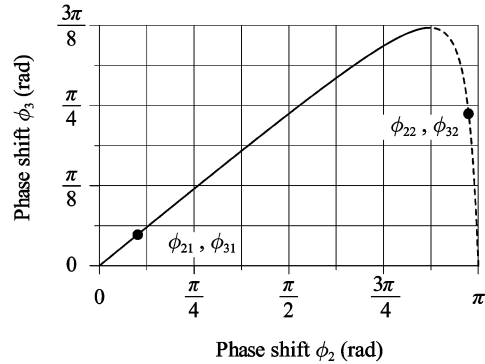


Fig. 7. Dependency of phase shift ϕ_3 on phase shift ϕ_2 for achieving zero net power flowing to port 3, i.e., $P_3 = 0$.

C. Control With One Port at Zero Average Power

An important feature of this three-port system is to directly supply power from one port, e.g., port 1, to another port, e.g., port 2, without charging or discharging the energy storage element on the third port, e.g., port 3. This cannot be realized when the magnitude of u_3 is lower than that of u_1 and/or u_2 even if all power transistors of port 3 full-bridge cell are remaining in the off-state as the anti-parallel free-wheeling diodes would be forced into conduction by high full-bridge cell output voltages u_1 and/or u_2 . Therefore, ϕ_2 and ϕ_3 have to be selected properly in order to achieve $P_3 = 0$ and a given value of $P_1 = -P_2 = P$ (since the sum of the power of three voltage sources has to be zero, $P_1 + P_2 + P_3 = 0$, if the losses are neglected and a negative power value indicates that the power is absorbed by the corresponding port).

Here, again $\phi_2 > 0$, $\phi_3 > 0$, and $\phi_2 > \phi_3$ is assumed. For the power of the ports, we then have

$$\begin{aligned} P_1 &= \frac{\phi_2(\pi - \phi_2)V_1V_2L_3 + \phi_3(\pi - \phi_3)V_1V_3L_2}{2\pi^2 f_s(L_1L_2 + L_2L_3 + L_3L_1)} \\ P_2 &= \frac{\phi_2(\phi_2 - \pi)V_1V_2L_3 + (\phi_2 - \phi_3)(\phi_2 - \phi_3 - \pi)V_2V_3L_1}{2\pi^2 f_s(L_1L_2 + L_2L_3 + L_3L_1)} \\ P_3 &= \frac{\phi_3(\phi_3 - \pi)V_1V_3L_2 + (\phi_2 - \phi_3)(\pi - \phi_2 + \phi_3)V_2V_3L_1}{2\pi^2 f_s(L_1L_2 + L_2L_3 + L_3L_1)}. \end{aligned} \quad (3)$$

From (3), now the relation of P_1 and ϕ_2 and of ϕ_2 and ϕ_3 can be derived under the side condition of $P_3 = 0$ and $P_1 = -P_2 = P$. As shown in Figs. 6 and 7 for an example operating point

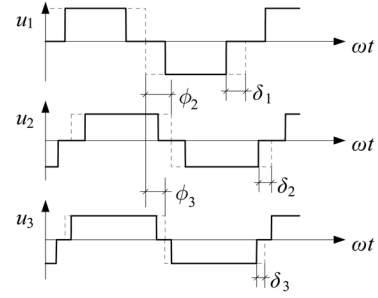


Fig. 8. Definition of phase displacements and duty cycles of the full-bridge cell output voltages u_1 , u_2 , and u_3 .

($P_3 = 0$ and $P_1 = -P_2 = 1$ kW with the electrical parameters shown in Table I) of the multiple voltage electrical system, there are two solutions (ϕ_{21}, ϕ_{31}) and (ϕ_{22}, ϕ_{32}) for ϕ_2 and ϕ_3 . As a set of higher phase shift values (ϕ_{22}, ϕ_{32}) results in a higher peak current in the leakage inductance and in higher conduction and switching losses, the lower phase shift values (ϕ_{21}, ϕ_{31}) are chosen for the system control.

III. MINIMIZATION OF THE OVERALL SYSTEM LOSSES

A. Introduction of the Duty Cycle Control

In order to gain degrees of freedom for minimizing the overall system losses, the duty cycle variation of the full-bridge cell output voltages u_1 , u_2 , and u_3 is introduced in addition to the phase shift control as shown in Fig. 8. The control range of δ_1 , δ_2 , and δ_3 is from 0 to $\pi/2$.

B. Zero Circulating Power

The power transferred from u_1 to u_2 , from u_2 to u_3 , and from u_3 to u_1 will be denoted as P_{12} , P_{23} , and P_{31} in the following. To aim for minimizing the system losses, the circulating power inside the system, which would not contribute to the power flow of the ports, has to be prevented, i.e.,

$$P_{12} + P_{23} + P_{31} = 0 \quad (4)$$

has to be ensured. Considering $P_2 = P_{21} + P_{23}$ and $P_3 = P_{31} + P_{32}$ with (4), we have P_{12} , P_{23} , and P_{31} in dependency on P_2 , P_3

$$\begin{aligned} P_{12} &= -\frac{2}{3}P_2 - \frac{1}{3}P_3 \\ P_{23} &= \frac{1}{3}P_2 - \frac{1}{3}P_3 \\ P_{31} &= \frac{1}{3}P_2 + \frac{2}{3}P_3. \end{aligned} \quad (5)$$

C. Range of ϕ_2 and ϕ_3

For controlling the system, five degrees of freedom, i.e., the phase displacements ϕ_2 and ϕ_3 and the duty cycles δ_1 , δ_2 , and δ_3 are available. Defining the power flows of two ports, e.g., P_2 and P_3 and ensuring zero circulating power, two degrees of

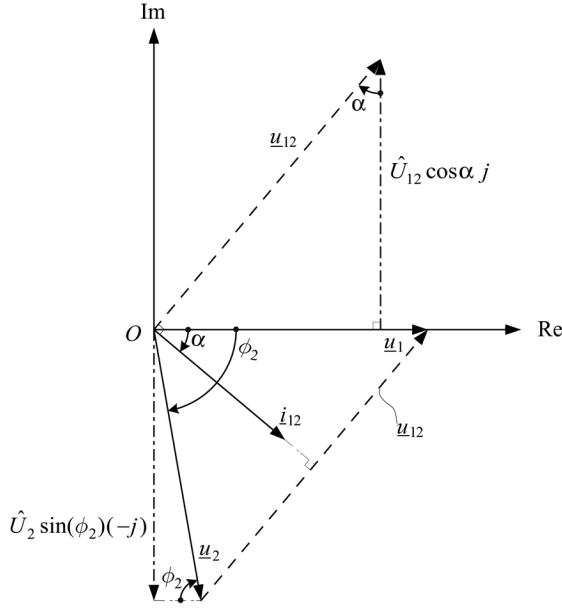


Fig. 9. Phasor diagram for the system voltages and currents.

freedom are remaining, i.e., the converter characteristics can be expressed in dependency on ϕ_2 and ϕ_3 .

For the sake of simplicity, the further considerations are restricted to the fundamental voltages and the fundamental currents. The corresponding phasor diagram is shown in Fig. 9, where \underline{u}_1 defines the orientation of the real axis $\underline{u}_1 = \hat{U}_1 + 0j$. Considering the phase displacement ϕ_2 of u_1 and u_2 , i.e., of \underline{u}_1 and \underline{u}_2 , \underline{u}_2 can be expressed as

$$\underline{u}_2 = \hat{U}_2 \cos(\phi_2) - \hat{U}_2 \sin(\phi_2)j. \quad (6)$$

Accordingly, \underline{u}_{12} formed by \underline{u}_1 and \underline{u}_2 is

$$\underline{u}_{12} = \underline{u}_1 - \underline{u}_2 = \hat{U}_1 - \hat{U}_2 \cos(\phi_2) + \hat{U}_2 \sin(\phi_2)j. \quad (7)$$

Introducing the phase displacement α of \underline{u}_1 and \dot{i}_{12} , \underline{u}_{12} which is leading \dot{i}_{12} by $\pi/2$ can be alternatively formulated as

$$\begin{aligned} \underline{u}_{12} &= \hat{U}_{12} \cos\left(\frac{\pi}{2} - \alpha\right) + \hat{U}_{12} \sin\left(\frac{\pi}{2} - \alpha\right)j \\ &= \hat{U}_{12} \sin(\alpha) + \hat{U}_{12} \cos(\alpha)j. \end{aligned} \quad (8)$$

Combining (7) and (8) results in

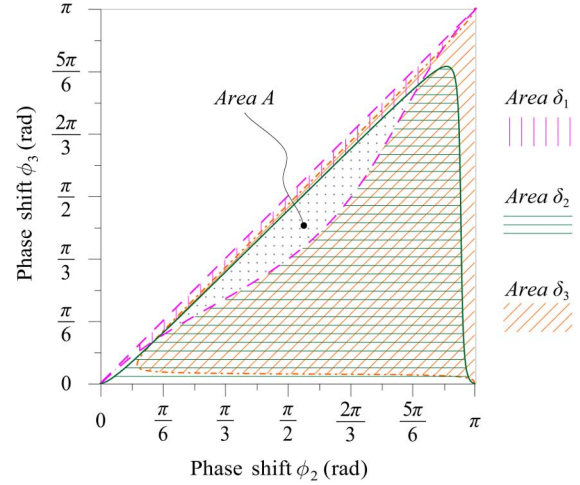
$$\hat{U}_2 \sin(\phi_2) = \hat{U}_{12} \cos(\alpha). \quad (9)$$

Considering (9), the power flow P_{12} now can be represented as

$$\begin{aligned} P_{12} &= \frac{1}{2} \hat{U}_1 \hat{I}_{12} \cos(\alpha) \\ &= \frac{1}{2} \hat{U}_1 \frac{\hat{U}_{12}}{\omega_s L_{12}} \cos(\alpha) \\ &= \frac{\hat{U}_1}{2\omega_s L_{12}} \hat{U}_{12} \cos(\alpha) \\ &= \frac{\hat{U}_1}{2\omega_s L_{12}} \hat{U}_2 \sin(\phi_2). \end{aligned} \quad (10)$$

Substituting $\hat{U}_1 = 4V_1 \cos(\delta_1)/\pi$, $\hat{U}_2 = 4V_2 \cos(\delta_2)/\pi$, and $\omega_s = 2\pi f_s$, in (10), P_{12} can be represented as

$$P_{12} = \frac{4}{\pi^3 f_s L_{12}} V_1 \cos(\delta_1) V_2 \cos(\delta_2) \sin(\phi_2). \quad (11)$$


 Fig. 10. Operating Area A, i.e., admissible range of phase shift ϕ_2 and phase shift ϕ_3 resulting from (13) with $P_1 = 1.5$ kW, $P_2 = -1$ kW, and $P_3 = -500$ W.

Analogously, we have P_{13} and P_{23}

$$P_{13} = \frac{4}{\pi^3 f_s L_{13}} V_1 \cos(\delta_1) V_3 \cos(\delta_3) \sin(\phi_3)$$

$$P_{23} = \frac{4}{\pi^3 f_s L_{23}} V_2 \cos(\delta_2) V_3 \cos(\delta_3) \sin(\phi_3 - \phi_2). \quad (12)$$

Referring to (11) and (12), the duty cycles δ_1 , δ_2 , and δ_3 now can be expressed as

$$\delta_1 = \begin{cases} \arccos(\Delta), & \text{if } (\phi_2 > \frac{\pi}{2}) \wedge (\phi_3 \leq \frac{\pi}{2}) \\ \pi - \arccos(\Delta), & \text{otherwise} \end{cases}$$

$$\delta_2 = \arccos\left(\frac{\pi^3 f_s P_{12} L_{12}}{4V_1 V_2 \cos(\delta_1) \sin(\phi_2)}\right)$$

$$\delta_3 = \arccos\left(\frac{\pi^3 f_s P_{13} L_{13}}{4V_1 V_3 \cos(\delta_1) \sin(\phi_3)}\right) \quad (13)$$

where

$$\Delta = \frac{\pi \sqrt{\pi f_s P_{12} P_{13} L_{12} (\tan(\phi_3) - \tan(\phi_2))}}{2V_1 \sqrt{P_{23} \tan(\phi_2) \tan(\phi_3)}}.$$

Taking into account the restriction that the argument of an inverse cosine function should be within $[-1, 1]$, (13) results in a limitation on the operating range of the converter and/or in a limitation on the admissible range of ϕ_2 and ϕ_3 . For example, there follows considering $\delta_1(\phi_2, \phi_3)$

$$-1 \leq \Delta \leq 1. \quad (14)$$

The corresponding range of ϕ_2 , ϕ_3 is denoted as Area δ_1 in Fig. 10. In analogy, Area δ_2 and Area δ_3 are resulting from $\delta_2(\phi_2, \phi_3)$ and $\delta_3(\phi_2, \phi_3)$. Considering all restrictions, the system operating area finally has to be restricted to Area A defined by the intersection of Area δ_1 , Area δ_2 , and Area δ_3 .

D. Power Loss Analysis

In this section, the losses in the power stage components are estimated. These losses can be categorized into two main parts: active component (MOSFET) losses and magnetic component losses. Any other passive component losses, such as capacitor losses and PCB losses, are neglected.

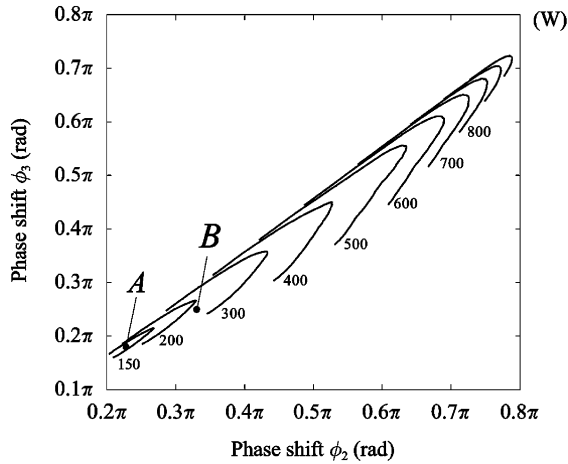


Fig. 11. Overall system losses in the whole admissible operating area *Area A* in dependency on ϕ_2 and ϕ_3 . One has to note, that operating point *A* is characterized by the minimum overall system losses. Operating parameters: as for Fig. 10.

1) *MOSFET Losses*: The two main power losses in MOSFETs are the conduction and switching losses. The conduction losses can be calculated straightforwardly from $P_c = I_{rms_M}^2 r_{ds}$, where r_{ds} is the on-resistance of MOSFET. Calculating the switching losses is more involved than calculating the conduction losses. The energy dissipated during one commutation can be estimated using a numerical solution of an equivalent circuit that includes the most relevant parasitic components such as the interterminal capacitances, and the source and drain inductances. A detailed discussion of this model is outside the scope of this paper.

2) *Magnetic Components Losses*: The main magnetic component in the converter is the transformer. Additionally, series inductors may also be needed if the transformer leakage inductances are so small that it is difficult to precisely control the phase shift angles required for transferring the demanded power. The power losses in the magnetic components consist of the core losses, which can be calculated by Steinmetz equation, and the winding losses, which can be estimated by the equations in [26] for Litz wire typically used in the 42- and 300-V windings and in [27] for copper foil typically used in the 14-V winding.

E. Optimum Operating Point

The overall system losses, which are composed of the conduction *and* switching losses of MOSFETs, and the core *and* winding losses of magnetic components can be evaluated numerically for every point in the whole admissible operating area *Area A*. In order to speed up the process and still to guarantee accuracy, a discrete grid is chosen, which divides the allowable range of the variable into 50 values and each value is then used in the numerical calculation. It should be noted that the allowable range of the dependent variable, e.g., ϕ_3 varies depending on the value of the independent variable, e.g., ϕ_2 in this case (cf. Fig. 10). The contour plot of the overall system losses for all grid points is illustrated in Fig. 11, for the particular power point as in Fig. 10 and the electrical parameters given in Table I. Fig. 11 shows that operating point *A* has lower overall system losses

TABLE I
ELECTRICAL PARAMETERS OF THE POWER STAGE

Description	Parameter
Port 1 dc voltage	$V_1 = 300$ V
Port 2 dc voltage	$V_2' = 42$ V
Port 3 dc voltage	$V_3' = 14$ V
Transformer turns ratios	$n_2 = 3/20$ $n_3 = 1/20$
Leakage inductances	$L_1 = 21$ μ H $L_2' = 495$ nH $L_3' = 55$ nH
Switching frequency	$f_s = 100$ kHz

compared to the other grid points. This is clearly verified by another operating point *B* which is characterized by significantly higher current amplitudes and higher voltage *and* current phase displacements and significantly higher losses (cf. Fig. 16). There is still one point which needs to be clarified is that any operating point featured by ϕ_2 and ϕ_3 is determined by the fundamental power, not the total power. Since the difference between these two powers is relative small, it is acceptable that the operating point is defined by the fundamental power.

IV. CONTROL STRATEGIES

A. Small Signal Model of the Three-Port Converter and Design of the Decoupling Network

As mentioned in Section III-C, two degrees of freedom, i.e., ϕ_2 and ϕ_3 are available as the control variables for the system control. For the multiple voltage electrical system in HEVs and FCVs where an energy storage element, such as a battery and/or supercapacitor, is connected to the bus to stabilize the bus voltage, it is desirable to control the charging/discharging current. Therefore, two port currents of the converter, e.g., I_2' and I_3' (cf. Fig. 13) could be the control objectives. The system could be considered as a two input (ϕ_2 and ϕ_3) and two output (I_2' and I_3') system.

However, it is difficult to build a full-order small signal model for the phase-shift controlled converter using the conventional state-space averaging technique since the ac current of the leakage inductance, whose average value over one switching cycle is always zero, cannot be a state variable in the model derived by using the state-space averaging method. It has been shown in [28] that a pole due to the inductor appears at high frequency, close to the converter switching frequency. Therefore, the influence by the inductor dynamics can be neglected if the model is used to predict low-frequency dynamics.

A simple approximate way to derive a control-oriented system model is to let the leakage inductances tend to zero. Assuming that system operating close to the optimum point *A* is ensured by the lookup tables where five degrees of freedom of the optimum operating point *A* can be obtained with the reference signals of I_2' and I_3' as the index parameters, the controller only has to slightly adjust the control variables, i.e., ϕ_2 and ϕ_3 in a given operating region. Accordingly, the small signal model of the three-port converter can be derived by linearization of the static control-to-output characteristic of the

converter around the operating point. The current I'_2 can be expressed according to (11) and (12)

$$\begin{aligned}
 I'_2 &= \frac{I_2}{n_2} \\
 &= \frac{P_{21} + P_{23}}{V_2 n_2} \\
 &= \frac{-P_{12} + P_{23}}{V_2 n_2} \\
 &= -\frac{4}{\pi^3 f_s L_{12} n_2} V_1 \cos(\delta_1) \cos(\delta_2) \sin(\phi_2) \\
 &\quad + \frac{4}{\pi^3 f_s L_{23} n_2} V_3 \cos(\delta_2) \cos(\delta_3) \sin(\phi_3 - \phi_2). \quad (15)
 \end{aligned}$$

The Taylor series of above port current I'_2 around the operating point A is

$$\begin{aligned}
 I'_2 &= I'_{2A} + \Delta I'_{2A} \\
 &= K_{1A} \sin(\phi_{2A}) + K_{2A} \sin(\phi_{3A} - \phi_{2A}) \\
 &\quad + K_{1A} \cos(\phi_{2A}) \Delta\phi_2 - K_{2A} \cos(\phi_{3A} - \phi_{2A}) \Delta\phi_2 \\
 &\quad + K_{2A} \cos(\phi_{3A} - \phi_{2A}) \Delta\phi_3 \\
 &= I'_{2A} + G_{11} \Delta\phi_2 + G_{12} \Delta\phi_3 \quad (16)
 \end{aligned}$$

where

$$\begin{aligned}
 G_{11} &= K_{1A} \cos(\phi_{2A}) - K_{2A} \cos(\phi_{3A} - \phi_{2A}) \\
 G_{12} &= K_{2A} \cos(\phi_{3A} - \phi_{2A}) \\
 I'_{2A} &= K_{1A} \sin(\phi_{2A}) + K_{2A} \sin(\phi_{3A} - \phi_{2A})
 \end{aligned}$$

with

$$\begin{aligned}
 K_{1A} &= -\frac{4}{\pi^3 f_s L_{12} n_2} V_1 \cos(\delta_{1A}) \cos(\delta_{2A}) \\
 K_{2A} &= \frac{4}{\pi^3 f_s L_{23} n_2} V_3 \cos(\delta_{2A}) \cos(\delta_{3A}).
 \end{aligned}$$

In analogy, the Taylor series of the port current I'_3 at the operating point A can also be obtained

$$I'_3 = I'_{3A} + G_{21} \Delta\phi_2 + G_{22} \Delta\phi_3 \quad (17)$$

where

$$\begin{aligned}
 G_{21} &= K_{4A} \cos(\phi_{3A} - \phi_{2A}) \\
 G_{22} &= K_{3A} \cos(\phi_{3A}) - K_{4A} \cos(\phi_{3A} - \phi_{2A}) \\
 I'_{3A} &= K_{3A} \sin(\phi_{3A}) - K_{4A} \sin(\phi_{3A} - \phi_{2A})
 \end{aligned}$$

with

$$\begin{aligned}
 K_{3A} &= -\frac{4}{\pi^3 f_s L_{13} n_3} V_1 \cos(\delta_{1A}) \cos(\delta_{3A}) \\
 K_{4A} &= \frac{4}{\pi^3 f_s L_{23} n_3} V_2 \cos(\delta_{2A}) \cos(\delta_{3A}).
 \end{aligned}$$

In summary, we have the small signal transfer function matrix of the converter

$$\Delta \mathbf{I}' = \begin{bmatrix} \Delta I'_2 \\ \Delta I'_3 \end{bmatrix} = \begin{bmatrix} G_{11} & G_{12} \\ G_{21} & G_{22} \end{bmatrix} \begin{bmatrix} \Delta\phi_2 \\ \Delta\phi_3 \end{bmatrix} = \mathbf{G} \Delta \Phi. \quad (18)$$

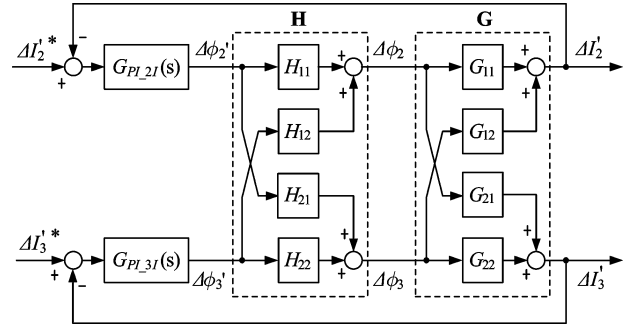


Fig. 12. Block diagram of the control system with the decoupling network. \mathbf{G} is the small signal transfer function matrix of the converter and \mathbf{H} denotes the transfer function of the decoupling network.

It can be observed that there is an interaction between two current loops, which can be eliminated via a special compensation network, that is a decoupling network \mathbf{H} . The role of decoupling network is to decompose a multivariable control system into a series independent single-loop subsystems. Thus, the system can be controlled using independent loop controllers, e.g., $G_{PI_2I}(s)$ and $G_{PI_3I}(s)$ in this case, depicted in the block diagram as Fig. 12, where the non-interacting decoupling control structure proposed in [29] is adopted.

In order to achieve independent control loops, i.e., $\mathbf{X} = \mathbf{G}\mathbf{H} = \text{diag}[x_1, x_2]$, the decoupling matrix could be designed as

$$\begin{aligned}
 \mathbf{H} &= \begin{bmatrix} H_{11} & H_{12} \\ H_{21} & H_{22} \end{bmatrix} \\
 &= \mathbf{G}^{-1} \\
 &= \begin{bmatrix} G_{11} & G_{12} \\ G_{21} & G_{22} \end{bmatrix}^{-1} \\
 &= \frac{1}{G_{11}G_{22} - G_{12}G_{21}} \begin{bmatrix} G_{22} & -G_{12} \\ -G_{21} & G_{11} \end{bmatrix}. \quad (19)
 \end{aligned}$$

Thus, $\mathbf{X} = \mathbf{G}\mathbf{H} = \mathbf{G}\mathbf{G}^{-1} = \text{diag}[1, 1]$. For every optimum operating point A , the small signal transfer function matrix \mathbf{G} of the converter is only a constant, i.e., no pole or zero is involved since the inductor dynamics are already neglected, and so does the decoupling network \mathbf{H} , which is the inverse matrix of \mathbf{G} . Therefore, based on the optimum operating point lookup tables mentioned above, the elements of the decoupling matrix can also be calculated in advance and be stored as lookup tables as well.

B. Implementation of the Control Strategy

Fig. 13 shows the implemented three-port system, where port 1 is connected with a voltage source $V_1 = 300$ V, port 2 is connected with an RC load, and port 3 is connected with an RC load parallel to a voltage source $V'_3 = 14$ V, therefore, this port can sink or source power or remain at zero power. L_{p1} , L_{p2} , and L_{p3} are the parasitic inductances (or possibly small bulky inductors) acting as parts of the C - L - C filters, which are used to limit the ripple currents flowing through the electrolytic capacitors in RC loads. Film/ceramic capacitors are placed near to the outputs of the full-bridge cells in order to absorb the high frequency ac ripple currents generated by the full-bridge cells

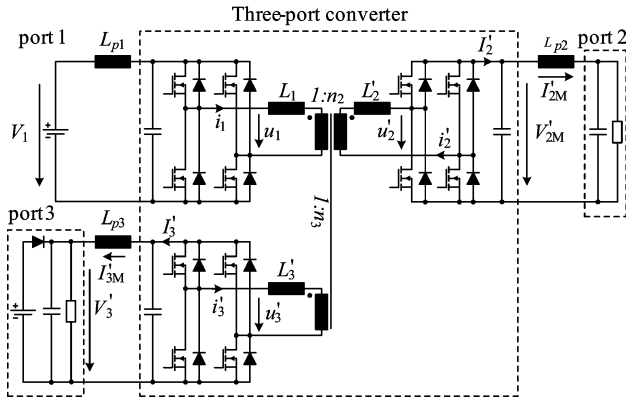


Fig. 13. Implemented three-port system. Port 1 is connected with a voltage source; port 2 is connected with an RC Load and port 3 is connected with an RC load parallel to a voltage source.

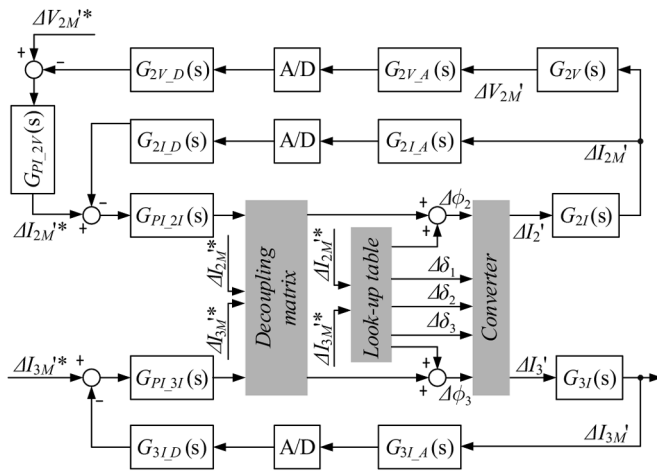


Fig. 14. Block diagram of the control loops in the implemented three-port system.

effectively. Therefore, I'_{2M} and I'_{3M} are measured instead of I'_2 and I'_3 , respectively. The output voltage V'_{2M} of port 2 is also regulated. Therefore, the whole control system includes two inner current loops and one outer voltage loop, as illustrated in the block diagram Fig. 14.

The control strategy is implemented in an Analog Devices ADSP-21992 160-MHz DSP and a Lattice ispMACH4512V CPLD. The values of five degrees of freedom, i.e., the phase displacements ϕ_2 and ϕ_3 and the duty cycles δ_1 , δ_2 , and δ_3 of the optimum operating point, are calculated numerically in advance and are stored in the DSP as lookup tables with the current reference signals as the index parameters. The elements of the decoupling matrix are also calculated in advance and stored in the DSP as lookup tables.

The DSP operates with a sampling frequency of 50 kHz for both the current and voltage control loops. The voltage V'_{2M} is first sampled by the internal 14-bit ADC and then the voltage controller generates the reference I'_{2M} for the inner current loop. The current reference values are used as the inputs to the multiple lookup tables to calculate the phase displacements and duty cycles. To generate higher precision output values from the lookup tables, the DSP uses linear interpolation rather than the

direct discrete values. Thus the system is then able to operate close to its optimal point. The outputs of the two phase shift angle lookup tables are adjusted by the controllers and manipulated by the decoupling network to eliminate the interaction between two current loops. Then together with the outputs of three duty cycle lookup tables, the five values are written into the CPLD where the correct 100-kHz PWM patterns are generated.

C. Control Loops of the Implemented Three-Port System

In the control system, there are three control loops, two inner current loops, and one outer voltage loop. The response of the voltage loop is slower than the current loops in order to minimize their interaction. This is one guideline for designing controllers. Here, we assume that the controllers are well designed and there is no interaction between these loops, i.e., the current loops and the voltage loop are totally decoupled. That is, the perturbation of the lookup tables caused by the perturbation of the output of the voltage loop, which is considered as a constant when analyzing the current loops, are neglected.

The transfer function of the control loop I'_{2M} illustrated in Fig. 14 with the consideration of the decoupling network is

$$G_{2I-T}(s) = G_{2I}(s)G_{2I-A}(s)G_{AD}(s)G_{2I-D}(s) \quad (20)$$

where $G_{2I}(s)$ denotes $I'_2(s)$ to $I'_{2M}(s)$ transfer function, $G_{2I-A}(s)$ and $G_{2I-D}(s)$ represent the anti-aliasing low-pass filter and the digital low-pass filter, $G_{AD}(s)$ is the transfer function of the sample and hold in the A/D converter. The current loop I'_{3M} and voltage loop V'_{2M} have the similar blocks, except $G_{2V}(s)$ which describes the RC load connecting to port 2.

The theoretical open-loop Bode plots of these loops of the three-port system are illustrated with dashed lines in Fig. 15, where it can be observed that the magnitude of the current loop I'_{2M} is kept constant at low frequency and starts to drop off beyond the lowest pole frequency of the digital filter. So a PI controller would be sufficient to regulate this loop. The zero of the PI controller is set around the lowest pole frequency in order to let the drop off in the magnitude of the Bode plot be -20 dB/dec at the gain crossover frequency and the proportional gain in the PI controller is suitably selected resulting in enough margin between the gain crossover frequency and the frequency where the drop off in the magnitude is -40 dB/dec. In a similar way, the PI controller for the control loop I'_{3M} can be designed. Due to the pole composed of the resistor and the capacitor in the RC load, the magnitude of the voltage loop V'_{2M} drops off earlier than that of the current loop I'_{2M} . The zero of the PI controller for the voltage loop is set around the pole caused by the RC load. The resulting open-loop Bode plots of these three loops including the PI controller are also shown in Fig. 15, where it can be found that the gain crossover frequencies of the two current loops are around 700 Hz and that of the voltage loop is around 100 Hz. Although the bandwidth of two current loops are close, their interaction would be eliminated by the decoupling network which will be verified in the experimental result section. The bandwidth of the current loop I'_{2M} is much higher than that of the voltage loop V'_{2M} , so the interaction between these two loops can be minimized. Therefore, these three loops can be controlled independently.

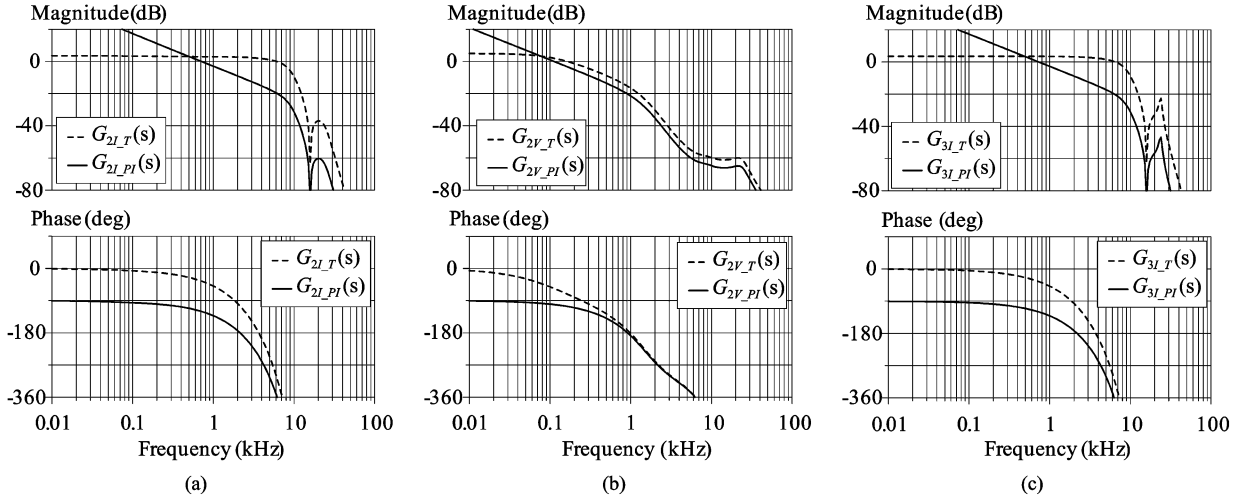


Fig. 15. Open-loop Bode plots of the three-port converter and those with corresponding PI controllers: (a) the current loop I_{2M}^* ; (b) the voltage loop V_{2M}^* ; (c) the current loop I_{3M}^* .

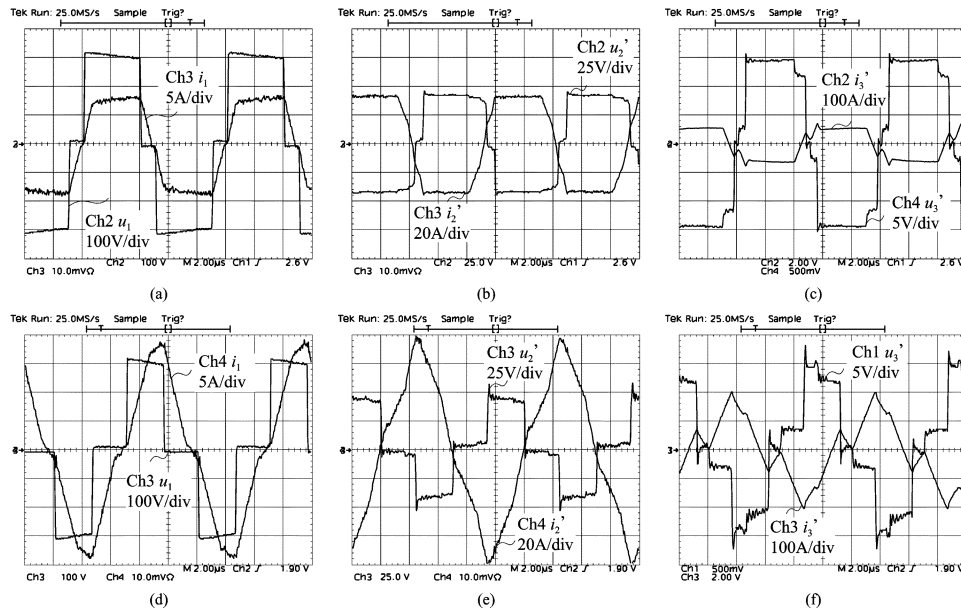


Fig. 16. Measured waveforms, showing the voltages between the phase leg midpoints in the full-bridge cells and the leakage inductance current of each winding with the reference signals $V_{2M}^* = 42$ V ($P_2^* = -1$ kW) and $I_{3M}^* = 35.7$ A ($P_3^* = -500$ W). (a)–(c) for the operating point A (cf. Fig. 11); (d)–(f) for the operating point B (cf. Fig. 11). One has to note, that the operating point A in general is characterized by the lowest system losses.

V. EXPERIMENTAL RESULTS

The previous theoretical considerations have been verified by an experimental setup whose circuit schematic of the power stage is illustrated in Fig. 13 with the electrical parameters given in Table I except V_2^* is the voltage of an RC load on port 2 instead of that of a voltage source.

Fig. 16 illustrates the measured steady-state operation results, showing the voltages between the phase leg midpoints in the full-bridge cells, i.e., u_1 , u_2 , and u_3 and the leakage inductance current of each winding, i.e., i_1 , i_2 , i_3 , with the reference signals $V_{2M}^* = 42$ V ($P_2^* = -1$ kW) and $I_{3M}^* = 35.7$ A ($P_3^* = -500$ W). The voltage waveforms are measured directly at the phase leg midpoints of the full-bridge cells, so the voltages of the lead inductances of MOSFET and the partly PCB layout inductances are excluded, resulting in the difference between the

oscilloscope recorded waveforms and the ideal ones, especially in the waveforms u_3 [cf. Fig. 16(c) and (f)] when the corresponding current i_3 changes rapidly.

These particular operating points (see Fig. 16) are the point A and the point B in Fig. 11. The converter has minimum overall system losses with the optimal operating point A, resulting in an efficiency 91.7%. By altering the operating point to the point B, where the converter has significantly higher current amplitudes (cf. Fig. 16), this leads to significantly higher losses and a resulting lower efficiency of 72.6%. Fig. 17 plots the measured converter efficiency of the optimum operating point A and it shows that the efficiency is above 90% over a wide range of output power (0 to 500 W for port 3 with $P_2^* = -1$ kW) and, therefore, the converter successfully operates with the minimum losses controller.

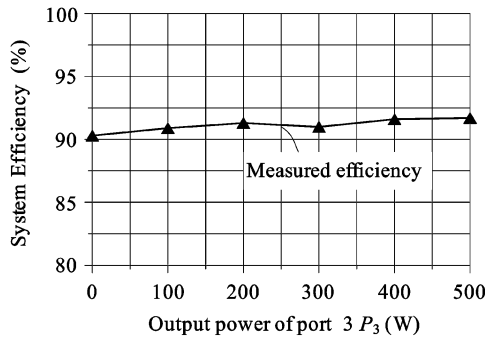


Fig. 17. Measured total system efficiency for different output power levels of port 3 with the reference signal $V_{2M}^* = 42$ V ($P_2^* = -1$ kW).

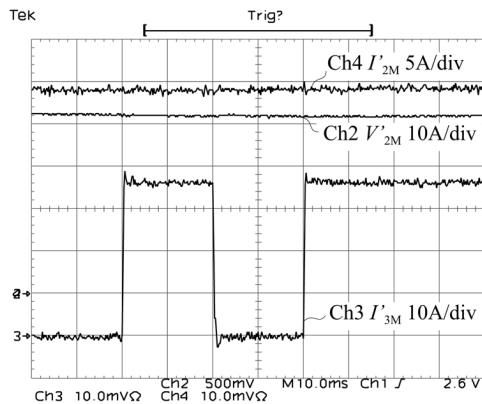


Fig. 18. Measured system dynamic behavior with the pulsating current reference signal $I_{3M}^* = 0$ A, $= 35.7$ A ($P_3^* = -500$ W), $= 0$ A and $= 35.7$ A, and the constant voltage reference signal $V_{2M}^* = 42$ V ($P_2^* = -1$ kW).

The measured system dynamic behavior, two port currents I_{2M}' and I_{3M}' and the voltage V_{2M}' of port 2 connecting an RC load in response to the current reference I_{3M}^* variations along with the constant voltage reference signal $V_{2M}^* = 42$ V ($P_2^* = -1$ kW), is shown in Fig. 18. At beginning the current reference signal I_{3M}^* is 0 A. It steps to 35.7 A ($P_3^* = -500$ W) and later steps back to 0 A. From the measured result, the voltage V_{2M}' and the current I_{2M}' are well regulated, always kept around the reference values. The control also shows excellent dynamics and no cross-coupling of the control loops is remaining, i.e., the variation of the current reference signal I_{3M}^* does not influence on the performance of another current loop I_{2M}' . Therefore, these control loops are regulated independently.

VI. CONCLUSION

In this paper, an isolated three-port bidirectional dc-dc converter formed by a single three-winding isolation transformer and corresponding full-bridge converter cells has been presented. The operating principle and optimization, steady-state analysis, small signal model, and control strategy were described. The experimental results for the 1.5 kW, 100-kHz prototype were shown to verify converter operation and power management features.

It is shown that the minimum overall system losses, no matter the port voltage has a fixed value or a wide range, is achievable by utilization of the duty cycle control combined with the

phase-shift control between the high-frequency ac voltages generated by the full-bridge cells. Controlling the power flow independently is implemented through the use of a decoupling network.

This converter is suitable for multiple voltage electrical systems where a storage element is required such as in renewable energy generation systems powered by solar and fuel cells.

REFERENCES

- [1] R. M. Schupbach, J. C. Balda, M. Zolot, and B. Kramer, "Design methodology of a combined battery-ultracapacitor energy storage unit for vehicle power management," in *Proc. IEEE Power Electron. Specialists Conf.*, Jun. 2003, vol. 1, pp. 88–93.
- [2] J. P. Barton and D. G. Infield, "Energy storage and its use with intermittent renewable energy," *IEEE Trans. Energy Convers.*, vol. 19, no. 6, pp. 441–448, Jun. 2004.
- [3] A. F. Burke, "Batteries and ultracapacitors for electric, hybrid, and fuel cell vehicles," *Proc. IEEE*, vol. 95, no. 4, pp. 806–820, Apr. 2007.
- [4] J. G. Kassakian, H. Wolf, J. M. Miller, and C. J. Hurton, "The future of automotive electrical systems," in *Proc. IEEE Workshop Power Electron. Transportation*, Oct. 1996, pp. 3–12.
- [5] J. Neubert, "Powering up [42 V automotive electronics]," *IEE Review*, vol. 46, no. 5, pp. 21–25, Sep. 2000.
- [6] K. Rajashekar, "42 V architecture for automobiles," in *Proc. Elect. Insulation Conf. Elect. Manufact. Coil Winding Technol. Conf.*, Sep. 2003, pp. 431–434.
- [7] I. A. Khan, "Automotive electrical systems: Architecture and components," in *Proc. Digit. Avionics Syst. Conf.*, Oct. 1999, vol. 2, pp. 8.C.5-1–8.C.5-10.
- [8] H. Matsuo, W. Lin, F. Kurokawa, T. Shigemizu, and N. Watanabe, "Characteristics of the multiple-input DC-DC converter," *IEEE Trans. Ind. Electron.*, vol. 51, no. 3, pp. 625–631, Jun. 2004.
- [9] Y.-M. Chen, Y.-C. Liu, and F.-Y. Wu, "Multi-input DC/DC converter based on the multiwinding transformer for renewable energy applications," *IEEE Trans. Ind. Appl.*, vol. 38, no. 4, pp. 1096–1104, Aug. 2002.
- [10] D. Liu and H. Li, "A ZVS bi-directional DC-DC converter for multiple energy storage elements," *IEEE Trans. Power Electron.*, vol. 21, no. 5, pp. 1513–1517, Sep. 2006.
- [11] H. Pinheiro and P. K. Jain, "Series-parallel resonant UPS with capacitive output DC bus filter for powering HFC networks," *IEEE Trans. Power Electron.*, vol. 17, no. 6, pp. 971–979, Nov. 2002.
- [12] C. Zhao and J. W. Kolar, "A novel three-phase three-port ups employing a single high-frequency isolation transformer," in *Proc. IEEE Power Electron. Specialists Conf.*, Jun. 2004, vol. 6, pp. 4135–4141.
- [13] J. L. Duarte, M. Hendrix, and M. G. Simoes, "Three-port bidirectional converter for hybrid fuel cell systems," *IEEE Trans. Power Electron.*, vol. 22, no. 2, pp. 480–487, Mar. 2007.
- [14] G.-J. Su and F. Z. Peng, "A low cost, triple-voltage bus DC-DC converter for automotive applications," in *Proc. IEEE Appl. Power Electron. Conf.*, Mar. 2005, vol. 2, pp. 1015–1021.
- [15] G.-J. Su, J. P. Cunningham, and L. Tang, "A reduced-part, triple-voltage DC-DC converter for electric vehicle power management," in *Proc. IEEE Power Electron. Specialists Conf.*, 2007, pp. 1989–1994.
- [16] H. Tao, A. Kotsopoulos, J. L. Duarte, and M. A. M. Hendrix, "Multi-input bidirectional DC-DC converter combining DC-link and magnetic-coupling for fuel cell systems," in *Proc. IEEE Ind. Appl. Conf.*, Oct. 2005, vol. 3, pp. 2021–2028.
- [17] H. Al-Atrash, F. Tian, and I. Batarseh, "Tri-modal half-bridge converter topology for three-port interface," *IEEE Trans. Power Electron.*, vol. 22, no. 1, pp. 341–345, Jan. 2007.
- [18] H. Al-Atrash, M. Pepper, and I. Batarseh, "A zero-voltage switching three-port isolated full-bridge converter," in *Proc. IEEE Int. Telecommun. Energy Conf.*, Sep. 2006, pp. 1–8.
- [19] H. Al-Atrash and I. Batarseh, "Boost-integrated phase-shift full-bridge converter for three-port interface," in *Proc. IEEE Power Electron. Specialists Conf.*, Jun. 2007, pp. 2313–2321.
- [20] N. D. Benavides and P. L. Chapman, "Power budgeting of a multiple-input buck-boost converter," *IEEE Trans. Power Electron.*, vol. 20, no. 6, pp. 1303–1309, Nov. 2005.
- [21] F. Z. Peng, H. Li, G.-J. Su, and J. S. Lawler, "A new ZVS bidirectional DC-DC converter for fuel cell and battery application," *IEEE Trans. Power Electron.*, vol. 19, no. 1, pp. 54–65, Jan. 2004.

- [22] R. W. A. De Doncker, D. M. Divan, and M. H. Kheraluwala, "A three-phase soft-switched high-power-density DC/DC converter for high-power applications," *IEEE Trans. Ind. Appl.*, vol. 27, no. 1, pp. 63–73, Jan. 1991.
- [23] H. Tao, A. Kotsopoulos, J. L. Duarte, and M. A. M. Hendrix, "A soft-switched three-port bidirectional converter for fuel cell and supercapacitor applications," in *Proc. IEEE Power Electron. Specialists Conf.*, 2005, pp. 2487–2493.
- [24] H. Tao, A. Kotsopoulos, J. L. Duarte, and M. A. M. Hendrix, "Triple-half-bridge bidirectional converter controlled by phase shift and PWM," in *Proc. IEEE Appl. Power Electron. Conf.*, Mar. 2006, pp. 1256–1262.
- [25] A. Ganz, "A simple, exact equivalent circuit for the three-winding transformer," *IRE Trans. Component Parts*, vol. 9, no. 4, pp. 212–213, Dec. 1962.
- [26] M. Bartoli, N. Noferi, A. Reatti, and M. K. Kazimierczuk, "Modeling Litz-wire winding losses in high-frequency power inductors," in *Proc. IEEE Power Electron. Specialists Conf.*, 1996, vol. 2, pp. 1690–1696.
- [27] R. W. Erickson and D. Maksimovic, *Fundamentals of Power Electronics*, 2nd ed. New York: Springer, 2001.
- [28] V. Vorperian, "Simplified analysis of PWM converters using model of PWM switch. II. Discontinuous conduction mode," *IEEE Trans. Aerosp. Electron. Syst.*, vol. 26, no. 3, pp. 497–505, May 1990.
- [29] W. L. Luyben, "Distillation decoupling," *AICHE*, vol. 16, no. 2, pp. 198–203, Mar. 1970.



Chuanhong Zhao (S'03) received the B.E. and M.E. degrees in electrical engineering from Zhejiang University, Zhejiang, China, in 2000 and 2003, respectively. She is currently working toward the Ph.D. degree in at the Power Electronic Systems Laboratory, Swiss Federal Institute of Technology (ETH) Zurich, Switzerland.

Her research interests include topologies, modulation, modelling, and control of bidirectional dc-dc converters.



Simon D. Round (SM'01) received the B.E. (honors) and Ph.D. degrees from the University of Canterbury, Christchurch, New Zealand, in 1989 and 1993, respectively.

From 1992 to 1995, he held positions of Research Associate in the Department of Electrical Engineering, the University of Minnesota, Minneapolis, and Research Fellow at the Norwegian Institute of Technology, Trondheim, Norway. From 1995 to 2003, he was a Lecturer/Senior Lecturer with the Department of Electrical and Electronic Engineering,

University of Canterbury, where he performed research on power quality

compensators, electric vehicle electronics, and cryogenic power electronics. He has also worked as a power electronic consultant for Vectek Electronics, where he developed a "state-of-the-art" digital controller for high-power inverter systems. In September 2004, he joined the Power Electronic Systems Laboratory at ETH Zurich, Switzerland, as a Senior Researcher. His current research interests are in ultra-compact power converters, digital control, medium voltage and high temperature applications of silicon carbide power devices, and the application of sparse matrix converters. He has over 90 publications in journals and international conferences. He has been actively involved in the IEEE New Zealand South Section, where he was Vice-Chair and Chairman from 2001 to 2004.

Dr. Round was a recipient of a University of Canterbury Teaching Award in 2001.



Johann W. Kolar (SM'04) received the Ph.D. degree (*summa cum laude/promotio sub auspiciis praesidentis rei publicae*) from the University of Technology Vienna, Vienna, Austria.

Since 1984, he has been an Independent International Consultant in close collaboration with the University of Technology Vienna in the fields of power electronics, industrial electronics, and high-performance drives. He has proposed numerous novel PWM converter topologies and modulation and control concepts, e.g., the VIENNA rectifier and

the three-phase ac-ac sparse matrix converter. He was appointed Professor and Head of the Power Electronic Systems Laboratory, Swiss Federal Institute of Technology (ETH), Zurich, Switzerland, in February 2001. In 2006, the European Power Supplies Manufacturers Association (EPSMA) awarded the Power Electronics Systems Laboratory of ETH Zurich as the leading academic research institution in Europe. The focus of his current research is on ac-ac and ac-dc converter topologies with low effects on the mains, e.g., for power supply of telecommunication systems, More-Electric-Aircraft, and distributed power systems in connection with fuel cells. Further main areas of research are the realization of ultra-compact intelligent converter modules employing latest power semiconductor technology (SiC), novel concepts for cooling and EMI filtering, multidomain/multiscale modelling and simulation, pulsed power, bearingless motors, and Power MEMS. He has published over 250 scientific papers in international journals and conference proceedings and has filed more than 70 patents.

Dr. Kolar was a recipient of the Best Transactions Paper Award of the IEEE Industrial Electronics Society in 2005 and an Erskine Fellowship from the University of Canterbury, New Zealand, in 2003. He is a Member of the IEEJ and of the Technical Program Committees of numerous international conferences in the field (e.g., Director of the Power Quality Branch of the International Conference on Power Conversion and Intelligent Motion). From 1997 through 2000, he served as an Associate Editor of the IEEE TRANSACTIONS ON INDUSTRIAL ELECTRONICS and since 2001 as an Associate Editor of the IEEE TRANSACTIONS ON POWER ELECTRONICS. Since 2002, he has been an Associate Editor of the *Journal of Power Electronics* of the Korean Institute of Power Electronics and a member of the Editorial Advisory Board of the *IEEJ Transactions on Electrical and Electronic Engineering*.